Ore Geology Reviews 107 (2019) 532–545

Contents lists available at ScienceDirect

Ore Geology Reviews

journal homepage: www.elsevier.com/locate/oregeorev

Selective crystallization and precipitation of authigenic pyrite during diagenesis in uranium reservoir sandbodies in Ordos Basin

Liang Yue[a], Yangquan Jiao[a,*], Liqun Wu[a], Hui Rong[a], Huili Xie[b], Qianyou Wang[c], Qianqian Yan[d]

[a] Key Laboratory of Tectonics and Petroleum Resources (China University of Geosciences), Ministry of Education, Wuhan 430074, China
[b] CNNC Beijing Research Institute of Uranium Geology, Beijing 100029, China
[c] Institue of Unconventional Natural Gas Research, China University of Petroleum, Beijing 102249, China
[d] Inner Mongolia Geology Engineering Co., Ltd., Huhhot 010010, China

ARTICLE INFO

Keywords:
Authigenic pyrite
Diagenesis
$\delta^{34}S$
Uranium reservoir
Zhiluo Formation
Ordos Basin

ABSTRACT

The occurrence characteristics of authigenic pyrite during diagenesis in uranium reservoir sandbodies of Zhiluo Formation in Ordos Basin are investigated. Based on outcrop area investigations and drilled cores observations, the pyrite is closely related to carbonaceous debris. Microscopically, the host components for pyrite consist of carbonaceous debris, clay minerals, biotite, the earlier pyrite, and ilmenite by emphasizing on $\delta^{34}S$ values via LA-ICP-MS, as well as observing through optical microscope and scanning electron microscope equipped with energy dispersive spectroscope. Three kinds of distribution pattern of pyrite are classified as: (i) periphery; (ii) infilling; (iii) the combined form of the above two. *In-situ* micrometer-scale sulfur isotope analyses of pyrite demonstrated that broad-scale isotopes are heterogeneous (from −52.5‰ to +35.4‰ of $\delta^{34}S$) and sulfur is derived from more than a single source. Significant differences of host components effects on authigenic pyrite formation are discussed. The carbonaceous debris can supply the energy for the bacterial sulfate reduction process, and the biotite can provide the source of iron for pyrite precipitation. The ferrous ion can be adsorbed on the surface of the clay minerals. Meanwhile, the authigenic pyrite is distributed in or around the earlier pyrite and ilmenite by the indirect adsorption of ferrous ion, and the ilmenite may also provide the source of iron. Futhermore, the uranium minerals are mainly associated with the authigenic pyrite relevant to carbonaceous debris and clay minerals, which indicates there exists constraints of authigenic pyrite during diagenesis on the uranium mineralization.

1. Introduction

The resistate mineral pyrite is the most common sulfide mineral and one of the most important components in various uranium-bearing mineral assemblages in sandstone-type uranium deposits (Nash et al., 1981; Min et al., 2005a; Scott, 2007; Ingham et al., 2014). Pyrite, widely developed in reductive sandbodies, is generally considered as an indicator for redox environment (Wignall et al., 2009; Wei et al., 2016), and also enhances the reducibility of reservoir (e.g., Cai et al., 2007; Miao et al., 2010a; Rong et al., 2016). Not only could the pyrite be one of the reductants making the dissolved hexavalent uranium [U(VI)] transform into insoluble tetravalent uranium [U(IV)] which precipitates immediately (e.g., Jensen, 1958; Granger and Warren, 1974; Chen and Guo, 2007; Laduke, 2013; Gallegos et al., 2015), it also plays a role of adsorbent making the uranium adhere to the surface of its particles being weathered or not (Goldhaber et al., 1987; Eglizaud et al., 2006; Qafoku et al., 2009; Miao et al., 2010b). However, data suggest that the reduction of pyrite during ore formation is very limited compared to organic matrix, CH_4, H_2S, etc (e.g., Spirakis, 1996). And the reduction will significantly decrease when the reaction temperature of fluids becomes slightly higher (Jensen, 1958; Rackley, 1972; Lach et al., 2015). The pyrite plays a more important role in the formation process (Warren, 1971; Cai et al., 2007; Lach et al., 2015), origin tracing (Shikazon, 1999; Min et al., 2005b; Akhtar et al., 2017) and ore prospecting (Northrop and Goldhaber, 1990; Scott et al., 2009; Zhang et al., 2017) of uranium deposit.

Studies of iron, sulfur and carbon geochemistry of modern sediments have led to a better understanding of pyrite formation mechanism (Warren, 1972; Raiswell and Berner, 1985; Raiswell, 1997; Wei et al., 2015). It is believed that the pyrite is the product from the chemical process of sulfide produced via bacterial sulfate reaction (Min et al., 2005b; Jaireth et al., 2010; Wei et al., 2013), with either Fe (II) in sediments or Fe (II) produced via bacterial Fe (III) reduction (Lovley et al., 1991; Canfield et al., 1992). And in this process, both hydrogen

* Corresponding author.
E-mail address: yueliang@cug.edu.cn (Y. Jiao).

https://doi.org/10.1016/j.oregeorev.2019.03.003
Received 3 May 2018; Received in revised form 26 January 2019; Accepted 4 March 2019
Available online 05 March 2019

sulfide and iron monosulfide are indispensable components to form varied morphologies of pyrite (Rickard, 1997; Butler and Rickard, 2000). Previous researches suggested that the pyrite in uranium reservoir sandbodies possesses multi-stages whose formation processes are complicated (Jiao et al., 2007; Chen and Guo, 2007; Chen et al., 2016), and whose formation origins are various in different areas (e.g., Ingham et al., 2014; Lach et al., 2015; Chen et al., 2016). Authigenic pyrite in the diagenetic process may have an inextricable connection with uranium minerals, and is one of the very important part of the big pyrite family.

Detailed observations of field outcrop and drilling cores from uranium ore deposits in northeastern and southern Ordos Basin to analyse the genesis of authigenic pyrite during diagenesis are carried out. In the uranium reservoir sandbodies, the pyrite has shown its multiple occurrence characteristics from both macroscopic and microscopic perspectives (Miao et al., 2010b; Chen et al., 2016). Past studies of XRD and geochemical analysis have demonstrated that the pyrite displayed extremely heterogeneous distribution in the same diagenetic environment, indicating that the mass percentage of pyrite in uranium reservoir sandbodies ranges from 0 to 11.1 wt%, with an average value of 1.8 wt %, lower than the contents of quartz, feldspar and clay minerals (Cai et al., 2007; Xie, 2016). In this paper, the diagenetic authigenic pyrite is chosen as the research object to analyse its occurrence characteristics and precipitation mechanisms based on sedimentological and geochemical theories. Microtextural analysis and *in-situ* sulfur isotope analysis of a suite of pyrite-bearing samples from the two uranium deposits show there exist preliminary constraints of authigenic pyrite on the uranium mineralization conditions and sources of diagenetic fluids for the uranium reservoir sandbodies in Ordos Basin.

2. Geological setting

The Ordos Basin containing abundant mineral resources such as coal, uranium, oil, natural gas and so on, is one of the most important energy source basins in China (Huang and Li, 2007; Li, 2007). There are two uranium deposits distributed in the northeastern named Dongsheng and the southern named Diantou respectively (Xiao et al., 2004; Chen et al., 2006; Li et al., 2008) (Fig. 1a).

The sandstone-type uranium deposit is hosted within the large-scale skeletal sandbodies in the Middle Jurassic Lower Zhiluo Formation (J_2z^1) classified into the lower parasequence set (J_2z^{1-1}) and the upper parasequence set (J_2z^{1-2}) (Fig. 1b). The lower parasequence set, originating from a type of braided river and braided river delta, is the primary ore-bearing stratum (Jiao et al., 2005a,b; Zhao and Ou, 2006; Zhang et al., 2010).

The Diantou uranium deposit is generated at the oxidation-reduction zone of shallow bury in the late period of burial diagenesis equivalent to epigenesis (Chen et al., 2006a,b; Li and Xu, 2006; Liu et al., 2007; Xing et al., 2008). However, the Dongsheng uranium deposit has experienced multistage uranium mineralization, and the processes can be divided into four main stages, namely preliminary enrichment during diagenesis, the interlayer oxidation during Late Jurassic to Paleocene, oil and gas reduction and ore preservation in the Early Cretaceous, and the transformation and superposition of ore bodies in the interlayer oxidation zone during Miocene to the present (Xiang et al., 2005, 2006; Han et al, 2008; Yang et al., 2009; Xue et al., 2011). Moreover, it is very common that the carbonaceous debris in the form of retention sediments occurs in the uranium reservoir sandbodies, enhancing the reducing power of sandstone to a great extent (Deditius et al., 2008; Jiao et al., 2018; Zhang et al., 2018). And the uranium minerals are mainly observed in the gray sandstone where a great deal of carbonceous debris and pyrite are well preserved (e.g., Cai et al., 2007; Miao et al., 2009).

3. Material and methods

Twenty samples of sandstone and pyrite nodules (SSG-01–14: different rock geochemical types of sandstone including purplish red, grayish green, yellow and gray sandtones; SSG-15–20: pyrite nodules) from outcrop combined with sixteen samples from different drilling wells were set in epoxy resin and prepared as polished thin sections for optical petrographic work with a Nikon ME600POL optical microscope, and then the sections were coated by carbon for both petrographic and mineralogical analysis by a EVO LS 15 scanning electron microscope equipped with the Aztec X-Max 20 energy dispersive spectrometer at the Key Laboratory of Tectonic and Petroleum Resources Ministry of Education at China University of Geosciences (CUG).

In-situ sulfur isotope analyses by Nu Plassma II Laser Ablation Multi-Collector Inductively Coupled Plasma Mass Spectrometry (LA-ICP-MS) were carried out using the Resolution S-155 laser at State Key Laboratory of Geological Processes and Mineral Resources at CUG. $^{34}S/^{32}S$ and $^{33}S/^{32}S$ ratios were measured under the conditions of light beam with 33 μm, 8 Hz and 50%T. The trace isotopes (^{34}S and ^{33}S) are related back to ^{32}S (Coplen et al., 2002; Johnston, 2011), following:

$$\delta^{3x}S = 1000 \times \left[\frac{(^{3x}S/^{32}S)_{sample}}{(^{3x}S/^{32}S)_{std}} - 1 \right] \quad (1)$$

where ^{3x}S refers to one of the minor isotopes. $(^{3x}S/^{32}S)_{sample}$ signifies the $^{3x}S/^{32}S$ of an unknown sample and $(^{3x}S/^{32}S)_{std}$ signifies the $^{3x}S/^{32}S$ value for the international standard VCDT. Different occurrence of pyrite grains were selected to text for variations in $\delta^{34}S$ and $\delta^{33}S$ summarized in Table 1.

Besides, four carbonaceous debris samples (ZK159-09–01–04) were selected to analyse its mineral characteristics at the Laboratory of Coal and Coalbed Methane at CUG. The carbonaceous debris was picked out using tweezers carefully for fear of combination with clastic particles and crushed to the grain diameter less than 0.2 mm, between 0.2 mm and 1 mm, respectively. Next, the two different components were mixed with the proportion of 1:5. Finally, the epoxy resin was added to the mixture by 1:5 in order to get a cylindrical sample. Similarly, polished section was needed to be coated by carbon for mineralogical analysis in the SEM.

4. Results

4.1. Morphological and textural observations

4.1.1. Macroscopical characteristics of authigenic pyrite

The pyrite grains are usually distributed nearby the carbonaceous debris (CD) in uranium reservoir sandbodies in the Shenshangou outcrop (Fig. 2). The fascinating phenomena have been observed that the majority of pyrite grains with larger diameter (commonly between 5 and 15 cm) are distributed near the unconformity interface between uranium reservoir sandbodies in Zhiluo Formation and the coal seam in Yan'an Formation (Fig. 2a), and the farther the distance between the pyrite grains and interface is, the smaller the diameter of pyrite will be. The banded CD with poor orientation at the bottom of sandbodies may be mainly derived from the coal seams which suffered the strong river scouring, and there are also many pyrite grains with a maximum diameter of 10 cm formed around it (Fig. 2b). The pyrite grain including some small carbonaceous debris is found between the two banded CD (Fig. 2c). In addition, a large number of small pyrite nodules are observed around the CD, and they are oxidized during epidiagenesis (Fig. 2d).

A few typical occurrence characteristics between pyrite and the CD in both cross and longitudinal section are observed in drilled cores (Fig. 3). The quantity and distribution state of pyrite appear to be controlled by the amount and activity of CD. And the boundary line between two components is indistinct because the pyrite taking up a

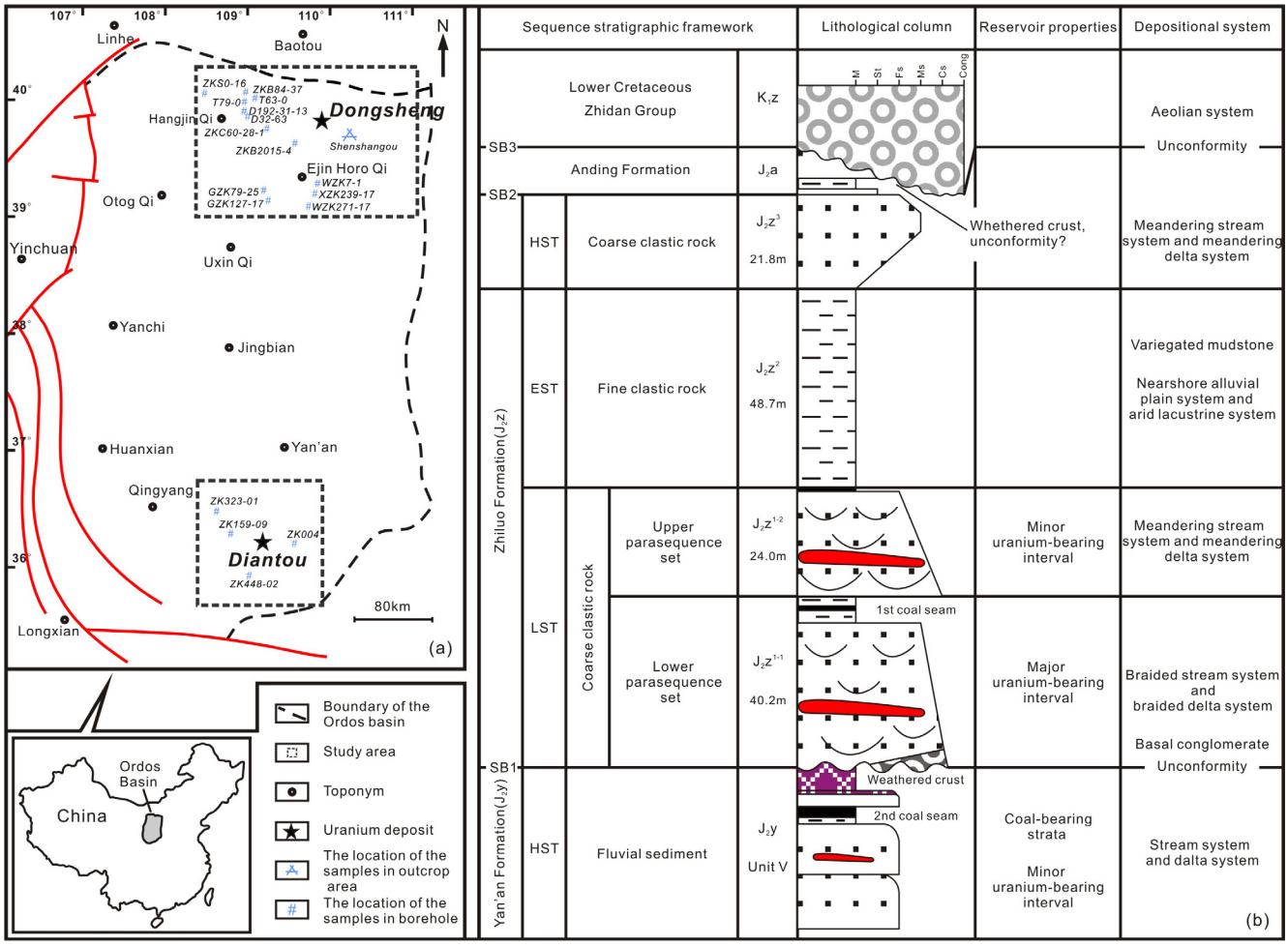

Fig. 1. Location of the study area in Ordos Basin and spatial relationship between the Jurassic sequence stratigraphic framework. (a). adapted from Liu (1998) and Ritts et al. (2004). (b). adapted from Jiao et al. (2016).

fraction of space of sandstone is disseminated near the CD (Fig. 3a). In longitudinal profile, the pyrite as the lenticular form developed upon CD is related genetically with CD apparently (Fig. 3b). It is a piece of gravel in the middle of the two lentiform pyrite grains that probably makes them not integrated perfectly. A part of pyrite grains of 2–5 cm in diameter approximately covers the banded CD, on which thin banded gypsum is distributed (Fig. 3c). In another borehole, the earlier pyrite nodule surrounded by a thin layer of the CD is observed. Most notably, the later pyrite (at the arrowhead) precipitates in the periphery of the CD, occupying a small amount of space (Fig. 3d).

4.1.2. Microscopical characteristics of authigenic pyrite

(1) Occurrence states

Our research shows that the components closely related to authigenic pyrite during diagenesis in uranium reservoir sandbodies can be divided into two categories, i.e., organic and inorganic constituents. The organic component is mainly presented as carbonaceous debris (CD), and inorgainc components are comprised of the clay minerals, biotite, pyrite formed earlier and ilmenite.

Table 1
Summary of data obtained during *in-situ* sulphur isotope analysis. δ Ratios represent a per mil deviation from the universal standard.

Point No.	Sample	Pyrite morphology	$^{34}S/^{32}S$	Error (E−05)	$\delta^{34}S$‰(VCDT)	$^{33}S/^{32}S$	Error(E-06)	$\delta^{33}S$‰(VCDT)	V
01	D192-31-13	Anhedral, assoc. uranium	0.050525	1.95	35.4	0.0084931	2.18	18.2	6.86
02	GZK127-17	Infill, assoc. biotite	0.049362	1.47	8.4	0.0083964	2.00	4.4	8.28
03	GZK79-25	Euhedral, assoc. clay minerals	0.048599	1.36	−2.8	0.0083467	2.12	−1.5	8.03
04	SSG-16	Cement, assoc. ilmenite	0.049844	0.41	18.2	0.0084385	2.61	9.5	6.25
05	SSG-19	Cement, assoc. ilmenite	0.049848	0.62	18.3	0.0084378	2.54	9.4	6.22
06	T79-0	Cement, assoc. uranium	0.046230	0.35	−52.5	0.0081211	1.67	−26.4	7.13
07	WZK271-17	Euhedral, assoc. clay minerals	0.049730	0.45	19.1	0.0084246	1.73	9.2	7.74
08	XZK239-17	Euhedral, assoc. clay minerals	0.048008	1.62	16.9	0.0084316	2.23	8.6	8.01
09	XZK7-1–01	Cement, assoc. carbonaceous debris	0.046520	0.40	−46.6	0.0081373	2.42	−24.4	6.97
10	XZK7-1–02	Cement, assoc. carbonaceous debris	0.046501	0.49	−47.0	0.0081427	2.13	−23.8	7.58
11	ZKB84-37-02	Cement, assoc. carbonaceous debris	0.047859	0.52	−19.2	0.0082649	1.97	−9.9	7.17
12	ZKB84-37-04	Infill, assoc. biotite	0.048039	1.13	−15.5	0.0082818	2.26	−7.9	7.47
13	ZKB84-37-05	Infill, assoc. carbonaceous debris	0.047765	0.39	−21.1	0.0082523	2.85	−11.4	6.42
14	ZKS0-16	Infill, assoc. biotite	0.047100	1.83	−37.8	0.0082076	2.36	−18.1	7.95

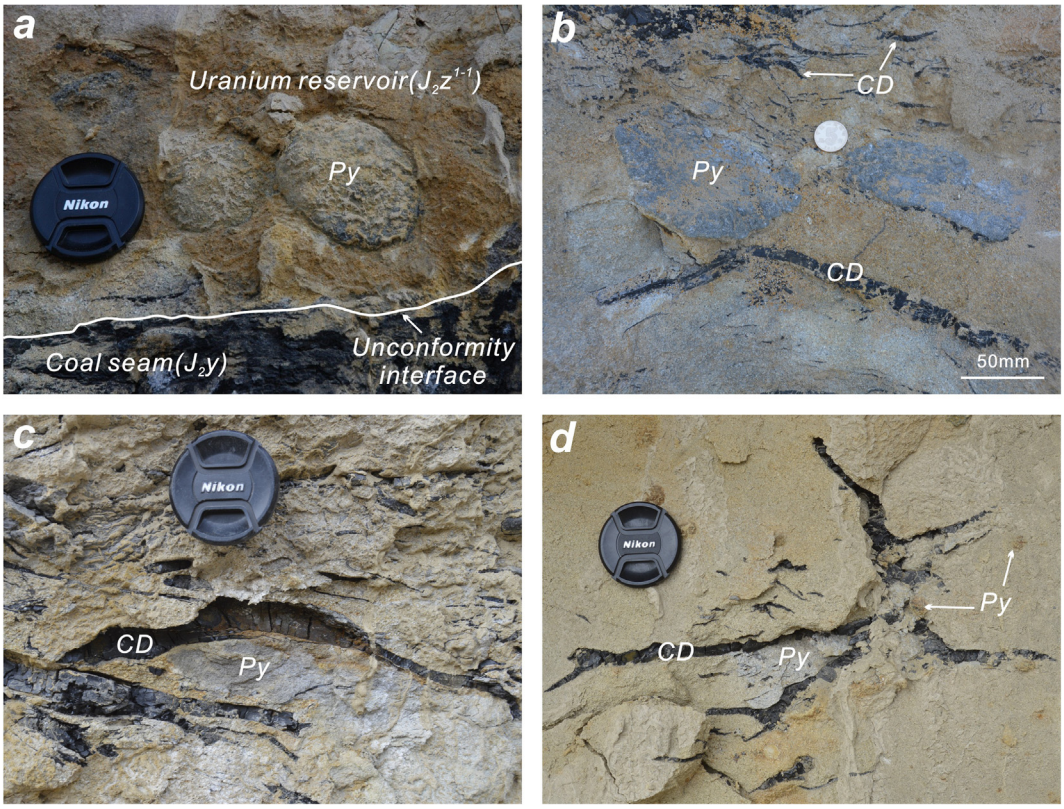

Fig. 2. Occurrence characteristics of pyrite (Py) in Shenshangou outcrop, Dongsheng uranium deposit. (a). The connection between the pyrite in uranium reservoir sandbodies in Zhiluo Formation (J_2z^{1-1}) with the coal seam in Yan'an Formation (J_2y); (b). The relationship between pyrite and carbonaceous debris (CD) in uranium reservoir sandbodies; (c). Pyrite grain is distributed between two banded CD. (d). The pyrite grain and many nodules are distributed around the CD.

Corresponding to those observed in outcrop and drilling cores, the distribution of pyrite is around or in the CD at the microscopical level (Fig. 4). In the view of transmission light, euhedral pyrite grain is formed around the banded CD, curved to a certain extent due to the compaction from pyrite crystallization (Fig. 4a). The another morphology is amorphous pyrite distributed around the CD, all of which fill in the matrix and the fracture of clastic particles (Fig. 4b). The banded CD is acting like a magnet, attracting the cement pyrite around it (Fig. 4c). Another specific state is that the amorphous pyrite filling in the CD, just the same as that of amorphous pyrite filling in the coal samples (Fig. 4d).

The inorganic constituents related to authigenic pyrite can be only observed under optical microscope, and that the role the clay minerals play should not be ignored (Fig. 5). The authigenic pyrite related with clay minerals is mainly present as octahedron (Fig. 5a and b) or cube (Fig. 5c and d), and is also partly as framboids which usually contain some trace elements (e.g. Ni, As, Se, etc) indicating the source of diagenetic fluids. Euhedral pyrite is preserved in the good crystalline form, which will be not influenced by later diagenetic fluids owing to the protection from calcite cementation (Fig. 5c and d).

It is prevalent that the pyrite fills in the cleavage of the biotite, and the morphologies are basically restricted by the direction of cleavage (Fig. 6). Because the biotite is easily to be deformed and altered during diagenesis, it will be distorted during the growth of the infilled pyrite (Fig. 6a). In the oxidized sandbodies, the pyrite filling in the cleavage is generally oxidized to Fe-oxides, whereas the core of mineral is well preserved (Fig. 6b). The euhedral pyrite can also be observed in the cleavage of the biotite around which abundant euhedral and cement pyrite are distributed (Fig. 6c). A few pyrite grains can be observed in the grayish green sandstone, however, because of the surrounding of biotite, the small pyrite grain can be prevent from the later supergene oxidation (Fig. 6d).

It is also found that the pyrite precipitates around the earlier pyrite grain, which makes the whole structure well ordered (Fig. 7). The pyrite morphology observed throughout the clay minerals is polyframboids which have gone through two evolution stages from microcrystals to framboids, and then to polyframboids comparable with those documented by Love (1971) (Fig. 7a). The framboidal state is probably best described as a metastable form, which can develop into euhedral pyrite under circumstances of abundant sources, while the framboid comparable with that put forward by Sawlowicz (1993) can be preserved in the core (Fig. 7b). In the pyrite nodules, the homogenous pyrite grain is isolated from other minerals, with some tiny particles of pyrite precipitate in the margins (Fig. 7c). It is a common phenomenon that the pyrite grain is surrounded by the later euhedral pyrite under certain conditions (Fig. 7d).

The last components related to diagenetic pyrite is the ilmenite, which is one of the most common heavy minerals in the sandstone (Fig. 8). Similarly to the CD, pyrite is mainly distributed in the fractures of the ilmenite, or around it (Fig. 8a). While the fractures are filled by other constituents in the earlier stage, the pyrite will fill the available space selectively (Fig. 8b). Significantly, the core of the ilmenite grain is filled with pyrite and Ti-oxides, but the edge of the grain is still the ilmenite (Fig. 8c). The same as the shape of the fractures, the pyrite fills in the space throughout the ilmenite in the pyrite nodule (Fig. 8d).

(2) Distribution pattern

Based on the relationship between diagenetic authigenic pyrite and the other components in sandbodies mentioned above, three kinds of distribution patterns are proposed and categorized as: (i) periphery; (ii) infilling; (iii) the combined form of the above.

One of the most prevalent distribution states, the pyrite is formed in the periphery of the other components (Fig. 9). The CD is not

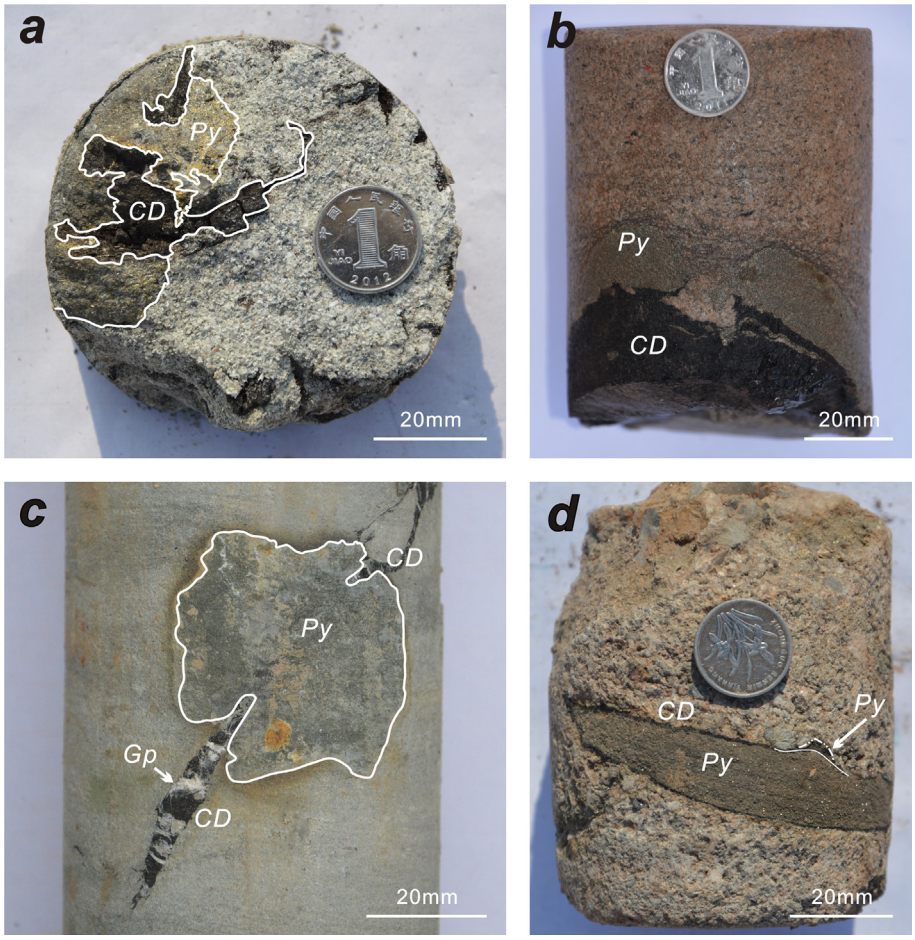

Fig. 3. Occurrence characteristics of pyrite (Py) in drilled cores. (a). Disseminated pyrite is distributed around the carbonaceous debris (CD), ZKB2015-4, 560.65 m, Dongsheng uranium deposit; (b). Pyrite grains are formed upon the carbonaceous debris, ZK004, 456.35 m, Diantou uranium deposit; (c). Pyrite grain covers the carbonaceous debris on which thin banded gypsum (Gp) is distributed, ZK448-02, 509.97 m, Diantou uranium deposit; (d). The pyrite grain is surrounded by CD, followed by the later pyrite, ZK323-01, 531.80 m, Diantou uranium deposit.

completely surrounded by the cement pyrite possibly due to the differences of physical properties in the sandbodies (Fig. 9a). In the oxidized sandbodies, the fine-grained pyrite produced around the clay minerals is well preserved without oxidation on account of the calcareous cements formed before oxidation (Fig. 9b). The pyrite is also distributed around the pyrite grain, and these two pyrite forms are not produced at the same time because the fine particles around the orthogonal pyrite in cross section appear to be euhedral (Fig. 9c). Similarly, the euhedral pyrite grain precipitates around the ilmenite filling with Ti-oxides, but the phenomenon is relatively rare (Fig. 9d).

Another existence form of authigenic pyrite during diagenesis is that the pyrite fills in the cleavages of the biotite, interstices of the microcrystals of framboids or the cells of the carbonaceous debris (Fig. 10). That the banded pyrite filling in the cleavages makes the biotite slightly deformed, and a conclusion could be drawn that the growing process of pyrite crystals has the characteristics of anisotropy (Fig. 10a). Due to the interstices between microcrystals, the frambiods will be developed more closely when the material sources of the iron and sulfur are abundant and the conditions are necessary (Fig. 10b). Another way of the infilling is to fill in the cell of the carbonaceous debris. Although the cellular structure is well preserved, the material compositions are competely destroyed by and replaced with pyrite mineral (Fig. 10c and d).

The last distribution pattern is that the pyrite is distributed not only in the fracture or cleavage of the minerals but also around the constituents (Fig. 11). Only when the source of pyrite is abundant can the existence form be observed. Obviously, the ilmenite is the most common constituents (Fig. 11). However, the earlier pyrite can also act as the host mineral.

4.2. Sulfur isotope compositions

Results of *in-situ* sulfur isotope analysis are summarized in Table 1. The $\delta^{34}S$ values are broadly heterogeneous, ranging from −52.5 to +35.4‰ (n−14). Distinct populations are recognized within this unusually broad range of values, which correlate with occurrence states of authigenic pyrite to some extent. The plot that $\delta^{34}S$ is against $\delta^{33}S$ demonstrates that there is a large variation in isotopic values from different horizons within the same uranium reservoir sandbodies (Fig. 12).

The $\delta^{34}S$ data of pyrite associated with carbonaceous debris ranges from −47.0‰ to −19.2‰. The sulfur isotope values recorded in pyrite filling in the biotite display a broader range of $\delta^{34}S$ (−37.8‰ to +8.4‰) and $\delta^{33}S$. However, the distribution of $\delta^{34}S$ values in pyrite grains associated with both clay minerals and ilmenite is in a relatively smaller range, from −2.8‰ to + 19.1‰, and +18.2‰ to +18.3‰ respectively. Because of the small size (< 33 μm) of the authigenic pyrite grain formed around the earlier pyrite grains, the sulfur isotope values can't be obtained, but this $\delta^{34}S$ data may be assumed a little different from those associated with clay minerals. Besides, the analysis results of $\delta^{34}S$ for the pyrite associated with uranium show a very broad range (−52.5‰ to +35.4‰).

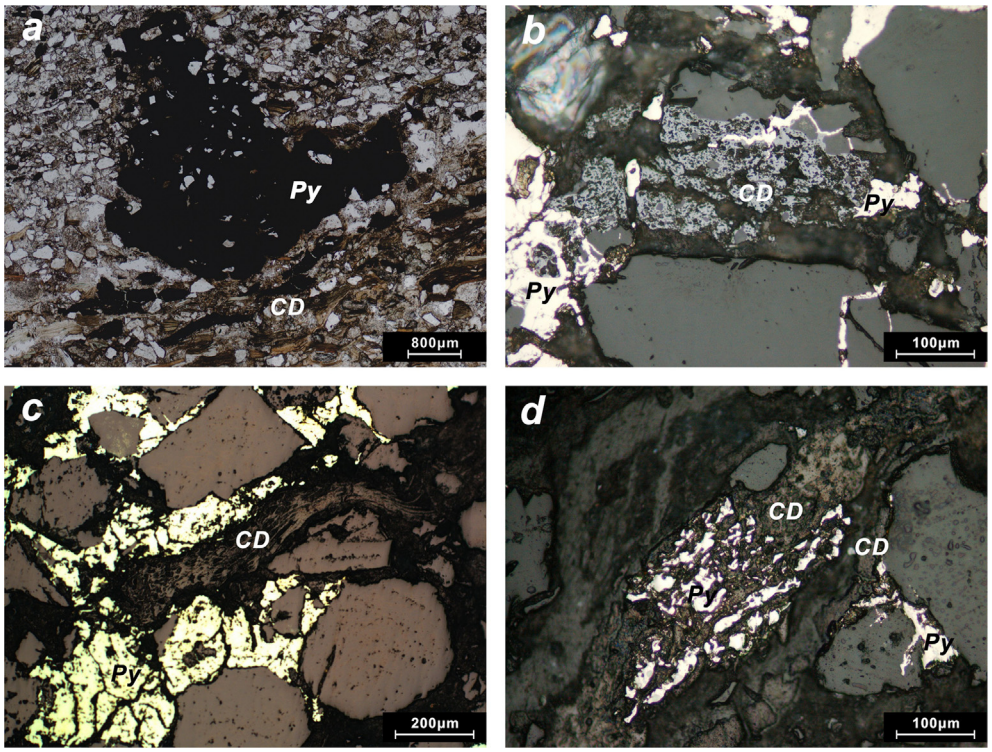

Fig. 4. Occurrence relationship between pyrite (Py) and carbonaceous debris (CD). (a). Euhedral pyrite grain is distributed around the banded carbonaceous debris, ZKB84-37-06, 398.54 m; (b). Amorphous pyrite is filled in the matrix and fracture of clastic particles around carbonaceous debris, ZKC60-28-01, 538.56 m; (c). The carbonaceous debris is almost surrounded by cement pyrite, ZKB84-37-02, 438.56 m; (d). The carbonaceous debris is filled with amorphous pyrite, ZKB84-37-05, 406.06 m.

5. Discussion

5.1. Origin of authigenic pyrite

The presence of pyrite with other components in the uranium reservoir sandbodies of Zhiluo Formation from outcrop area investigations, drilled cores observations and thin section analyses suggests that pyrite selectively precipitates from diagenetic fluids. Previous studies show that both Fe-dominated fluids and sulfate or sulfide are necessary to form pyrite during diagenesis (Butler and Rickard, 2000; Taylor and Macquaker, 2000; Min et al., 2005b).

During the diagenetic process, the dissolved Fe (III) from the fluids containing oxygen will be reduced to iron monosulfide completely when it reached a certain depth interpreted as the reducing

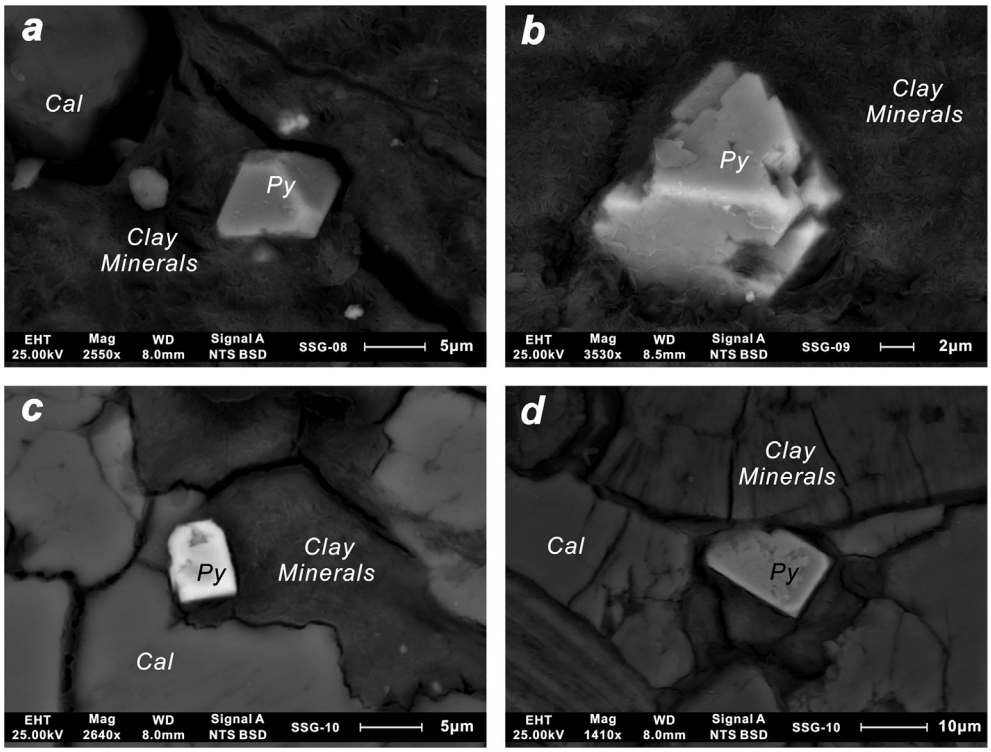

Fig. 5. Occurrence relationship between pyrite (Py) and the clay minerals. (a). Octahedral pyrite grain is distributed in the clay minerals surrounded by calcite (Cal); (b). Octahedral pyrite grain is surrounded by clay minerals; (c) and (d). Rectangular pyrite grain is preserved well in the clay minerals.

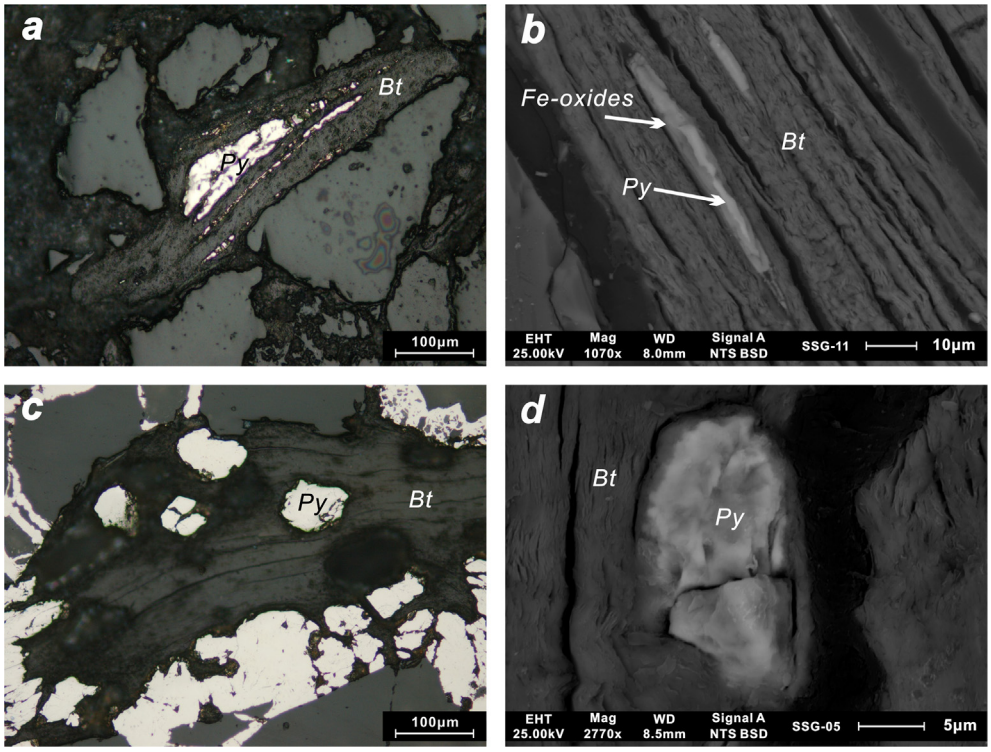

Fig. 6. Occurrence relationship between pyrite (Py) and biotite (Bt). (a). Pyrite fills in the cleavage of the biotite, ZKB84-37-04, 412.67 m; (b). Pyrite intergrows with Fe-oxides in biotite; (c). Euhedral pyrite grains are distributed in and around the biotite, ZKS0-16, 745.65 m; (d). The pyrite grain is absolutely surrounded by biotite.

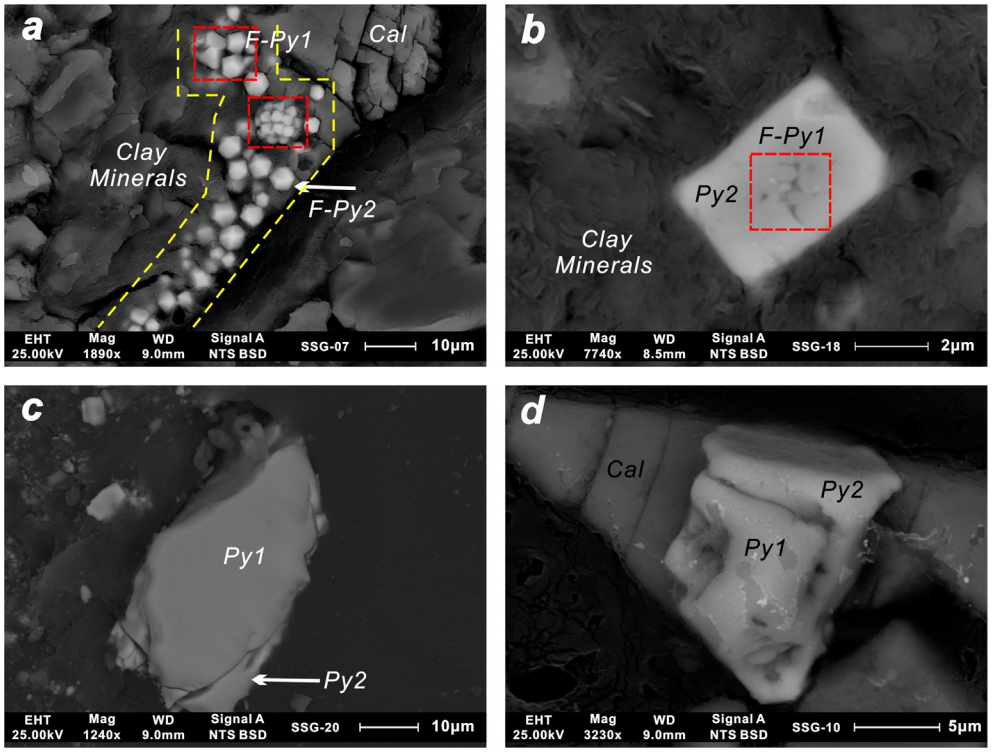

Fig. 7. Occurrence relationship between the earlier pyrite (Py1) and the later pyrite (Py2). (a). The framboids (F-Py1) and the plyframboids (F-Py2) are surrounded by clay minerals and calcite (Cal); (b). The core of the pyrite grain (Py2) is the framboidal pyrite (F-Py1); (c). Some tiny particles of pyrite (Py2) is found in the periphery of the pyrite grain (Py1); (d). The euhedral pyrite (Py2) is formed on the outside of the pyrite grain (Py1), surrounded by calcite.

environment in the uranium reservoir under the ground. At the same time, both the Fe (II) in sediments and the Fe (II) reduced by Fe (III) via reducing bacteria will react with hydrogen sulfide to produce iron monosulfide (e.g., Sweeney and Kaplan, 1973; Rickard, 1997; Butler and Rickard, 2000). And the reaction equations are described as follows, respectively:

$$O_2 + Fe^{3+} + H_2S + CH_4 \rightarrow SO_4^{2-} + FeS + CO_2 + H^+ \quad (2)$$

$$Fe^{2+} + H_2S \rightarrow FeS + 2H^+ \quad (3)$$

where FeS is an electroactive and dissolved species, and is one of the direct reactants to produce pyrite.

Moreover, no sulfur-rich organic matter is found in the uranium reservoir sandbodies in the area, and combined with the negative $\delta^{34}S$

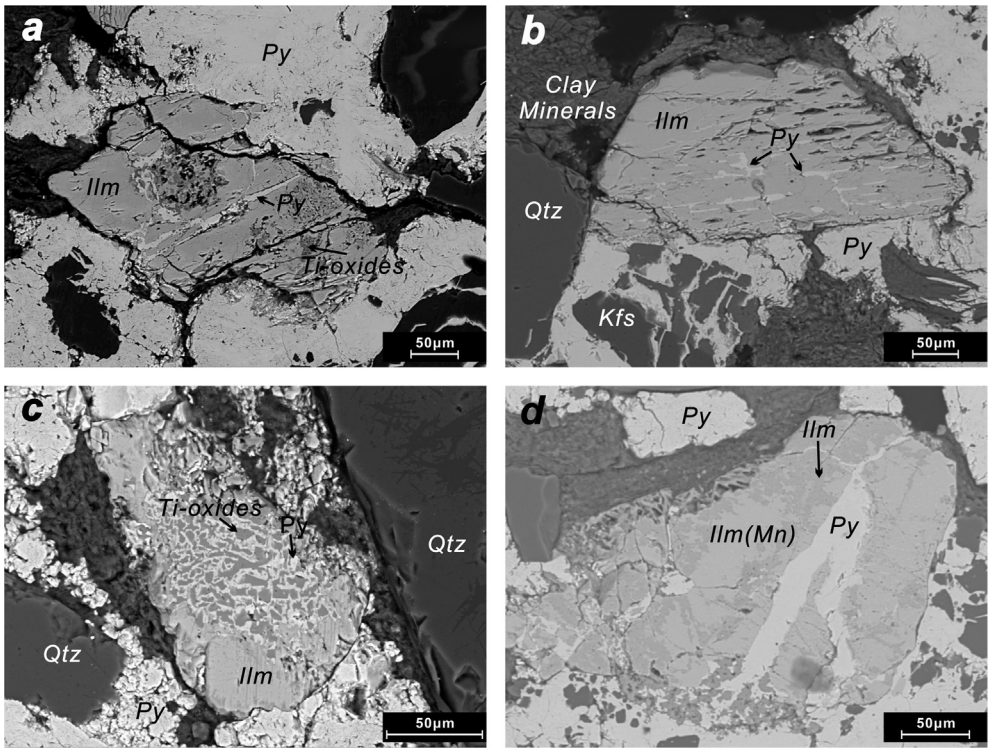

Fig. 8. Occurrence relationship between pyrite (Py) and ilmenite (Ilm). (a). The pyrite is distributed in and around the ilmenite grain, SSG-15; (b). The pyrite fills in the fractures without any other compositions in the earlier stage, SSG-19; (c). The pyrite and Ti-oxides fill in the core of the ilmenite, SSG-16; (d). The pyrite is distributed in the fracture throughout the ilmenite. Ilm(Mn)-the ilmenite containing manganese element, SSG-16. Qtz-quartz, Kfs-K-feldspar.

values as low as −52.5‰, which suggests that the sulfur with negative $\delta^{34}S$ values originates from the bacterial sulfate reduction (Cai et al., 2002, 2007). Sulfate-reducing bacteria preferentially utilizes sulfate with light sulfur (Chambers and Trudinger, 1979), and organic material in the sedimentary systems supplies the energy for the reduction (Warren, 1972; Beier and Feldman, 1991):

$$2[CH_2O] + SO_4^{2-} \rightarrow 2HCO_3^- + H_2S \quad (4)$$

in which CH_2O represents organic matter, including functionalized compounds such as carboxylic acids and alcohols (e.g., Jobson et al., 1979; Reynolds and Goldhaber, 1982; Raiswell and Berner, 1985).

Therefore, the pyrite will precipitate probably when both iron monosulfide and hydrogen sulfide are produced in or transported into the same locality at the same time (e.g., Guevremont et al., 1998; Cai et al., 2008), and the pyrite around the organic matter will have a negative $\delta^{34}S$ value. The reaction equation is described as follows:

$$FeS + H_2S \rightarrow FeS_2 + H_2 \quad (5)$$

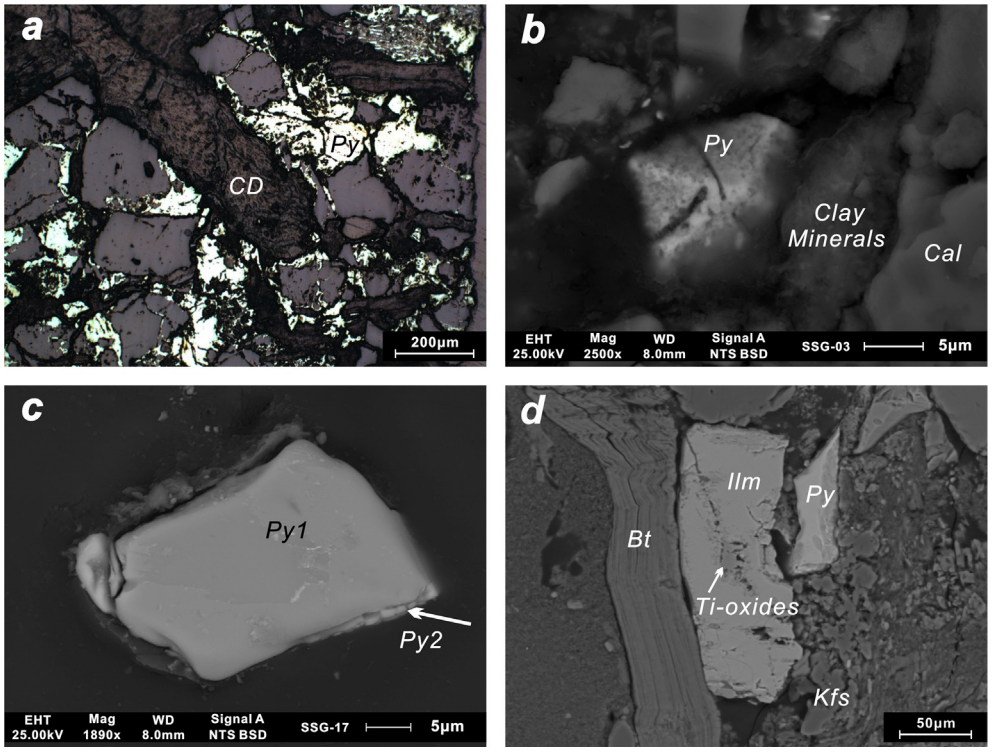

Fig. 9. The distribution pattern of pyrite (Py) formed in the periphery of other components. (a). Pyrite is distributed around the carbonaceous debris (CD), ZKB84-37-03, 424.85 m; (b). Pyrite is distributed around the clay minerals; (c). The fine pyrite fragment (Py2) is formed around the pyrite grain (Py1); (d). The pyrite grain is distributed in the periphery of the ilmenite (Ilm), with the Ti-oxides in the core, SSG-08. Bt-biotite, Cal-calcite, Kfs-K-feldspar.

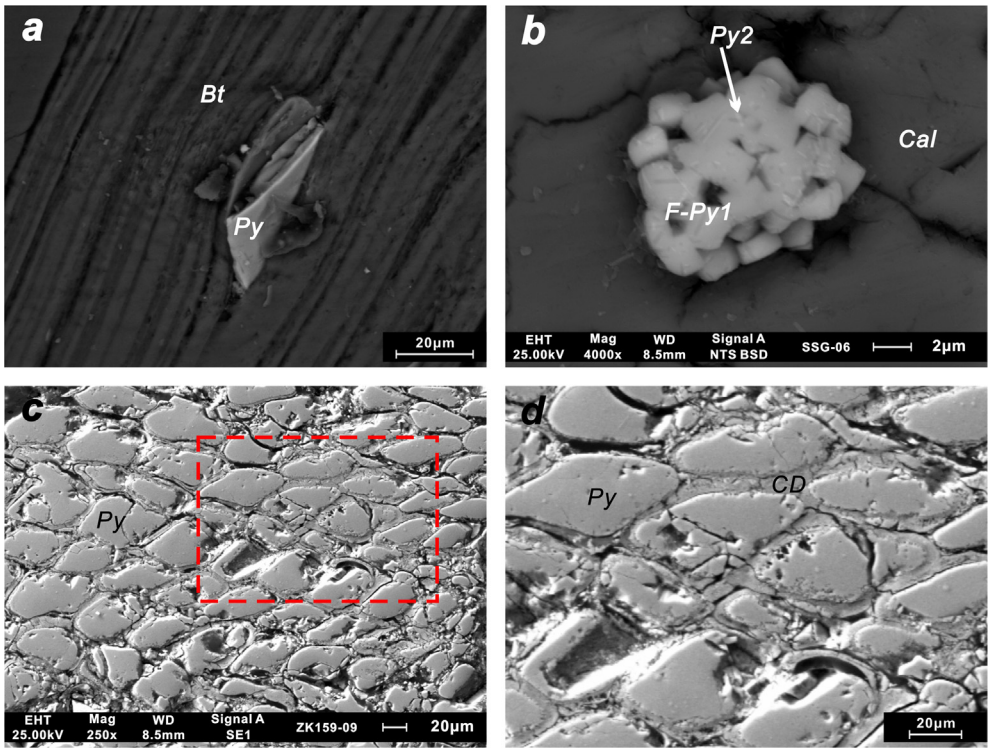

Fig. 10. The distribution pattern of pyrite (Py) filling in the other components. (a). Pyrite fills in the biotite (Bt), SSG-07; (b). The pyrite (Py2) fills in the interscites between microcrystals (F-Py1), surrounded by calcite (Cal); (c). The cells of carbonaceous debris with the infillings of pyrite, ZK159-09–04, 402.10 m; (d). The enlargement of the box in (c), C-organic matters.

Based on the above analyses, such components that are the source of iron or hydrogen sulfide, or have impacts on its occurrence states will affect the crystallization and precipitation of authigenic pyrite during diagenesis in the sandbodies.

The carbonaceous debris is the most closely related to pyrite and plays an important role in the process of uranium mineralization (Wulser et al., 2011; Riegler et al., 2016). The locality is generally regarded as the reducing microenvironment as long as the carbonaceous debris is well preserved (Kortenski and Kostova, 1996; Sun, 2016). As a kind of organic matters, the CD can supply the energy for the sulfate reduction to produce hydrogen sulfide, thus it will be easier to form pyrite around it and each one has a negative $\delta^{34}S$ value (−47.0‰ to −19.2‰) during diagenesis. Moreover, the different numerical value may represent the different degrees of the reduction.

Differently, previous researches have shown that the clay minerals possess a high specific surface area and a good adsorption performance (e.g., Wang and Zhao, 2012; Chen et al., 2015). Most of the pyrite grains occurred around the clay minerals display relative ^{34}S enrichment (+16.9‰ and +19.1‰). The dissolved ferrous iron may be adsorbed on the surface of the clay minerals from diagenetic fluids, and the authigenic pyrite will be produced when the hydrogen sulfide is supplied without the participation of microorganism or organic matters.

Compared with CD, the biotite containing iron can be the source for pyrite formation. And the cleavage in one direction provides the limited space for pyrite production and preservation. In general, the pyrite filling in the biotite has relatively positive $\delta^{34}S$ values (+8.4‰ in Point No.02), while the ^{34}S depletion in Point No. 12 (−15.5‰) and Point No.14 (−37.8‰) is characteristic of a biogenic sulfur source (Raiswell, 1982; Seal, 2006) because of the existence of CD at a short distance away from the biotite.

Although the iron-bearing minerals such as pyrite and ilmenite provide neither dissolved iron nor hydrogen sulfide for pyrite formation, the adsorption of pyrite and ilmenite on ferrous ion makes it easier to produce pyrite again around or filling in the earlier iron-bearing minerals (e.g., Butler and Rickard, 2000; Taylor and Macquaker, 2000). However, the phenomenon that both Ti-oxides and pyrite existed in the core of ilmenite makes it possible to provide the source of Fe for pyrite formation (Qiao et al., 2013). According to the sulfur isotope analysis, the pyrite mineralization is developed in an unbalanced open system

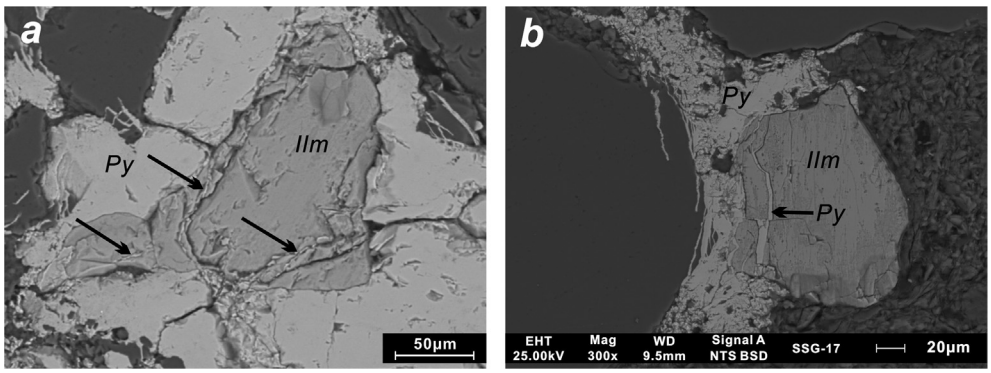

Fig. 11. The distribution pattern of pyrite (Py) distributed in and around the other components. (a). Pyrite is formed in the fractures of ilmenite (Ilm) and around it, SSG-15; (b). Pyrite is distributed in the fracture of ilmentite in which the fine grain of ilmenite is surrounded by cement pyrite (arrow), SSG-17.

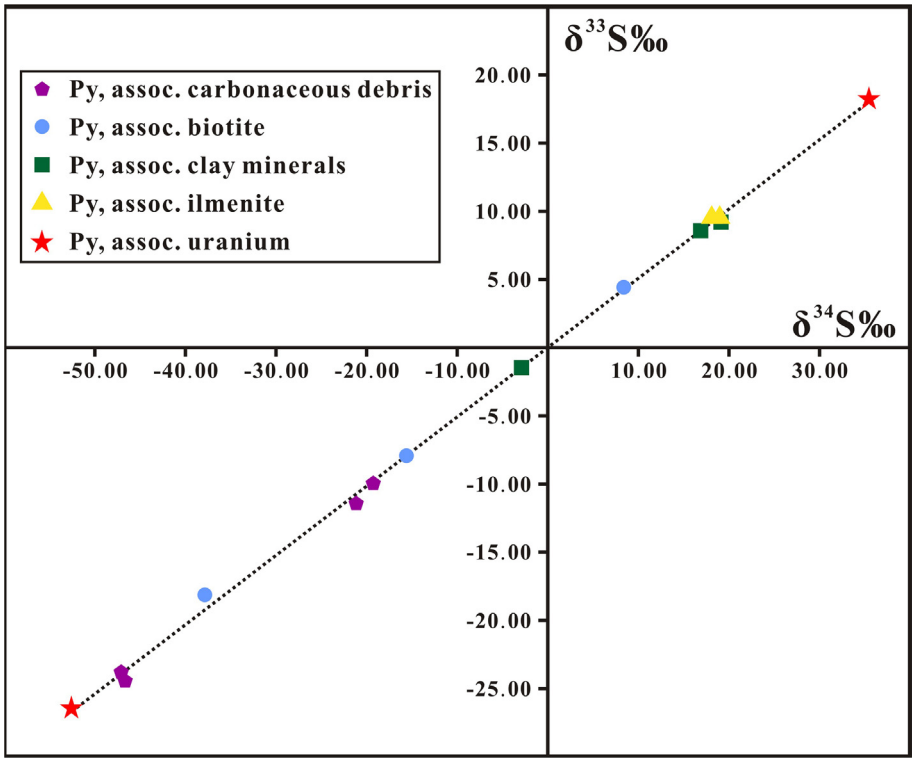

Fig. 12. $\delta^{34}S$ values are displayed against $\delta^{33}S$ values for each individual analysis. This plot can be used to extract information about the source of the sulfur. Despite the limited number of analyses per category of pyrite, a large variation of sulfur isotope compositions are recorded.

with a low temperature hydrothermal sulfur source (Kohn et al., 1998; Cai et al., 2007; Xue et al., 2010; Liang et al., 2017). Furthermore, the further researches need to be done in the future and to offer a comprehensive explanation.

5.2. The correlation between pyrite and uranium mineralization

The lower sulfur isotope value (−52.5‰, Table 1) of pyrite related to uranium minerals is more negative than the known lightest value of organically derived sulfur (Aplin and Coleman, 1995; Cai et al., 2002), which indicates that the sulfur with negative $\delta^{34}S$ can be originated from multi-step bacterial sulfate reduction (BSR), indicating a biogenic origin (Rackley, 1972; Ulrich et al., 2001; Cai et al., 2007; Jiang et al., 2016; Zhao et al., 2018), and the source of sulfate may be from groundwater and the Lower Cretaceous gypsum-bearing strata in Diantou uranium deposit (Cai et al., 2007). While the sulfur may be contributed from a hydrothermal source in an open system with positive $\delta^{34}S$ value (+35.4‰, Table 1) (Holser, 1977; Jiang and Ling, 2004; Seal, 2006; Zhao et al., 2018).

The study in both underground and outcrop uranium reservoir sandbodies found that the uranium minerals were closely associated with the authigenic pyrite distributed around or in the clay minerals and carbonaceous debris (Fig. 13). The clay minerals are mainly the products generated by the alteration of potash feldspar, and the uranium minerals are mainly coffinite due to the combination of dissolved quartz and ore fluids (Xiang et al., 2006; Miao et al., 2010b; Wu et al., 2016) (Fig. 13a–c). Because of the distribution of Ni, the framboids are generally interpreted as the products of the early diagenetic processes (Sawłowicz, 2000), and partially replaced by uranium minerals subsequently (Fig. 13d–f). The detection of minor Se in framboidal pyrite in carbonaceous debris in sample D32-63 (Dongsheng uranium deposit) provides an insight into late-stage mineralization processes (Fig. 13g), and noteworthily, the replacement is only found in the diagenetic framboidal pyrite (containing Ni and Se) controlled by carbonaceous debris and the clay minerals (Fig. 13h). And in the biotite, the uranium minerals seem to have a close relationship with altered biotite rather than the infilled pyrite (Yang et al., 2009; Miao et al., 2010b; Ma et al., 2013; Chen et al., 2017) (Fig. 13i). However, it was not observed that uranium minerals precipitated around the authigenic pyrite related to ilmenite or the earlier pyrite grain.

The uranium minerals are selective for the pyrite formed period, and the same to the categories of the authigenic pyrite during diagenesis, and the selectivity has the inextricably link with the forming time of uranium and internal flowing space in sandbodies. Previous studies show that the quantity of pyrite in mineralization zone is significantly more than that in oxidation zone and reduction zone, which indicates abundant authigenic pyrite is produced in the processes of uranium metallogenesis (Yi et al., 2015a,b; Chen et al., 2016; Yi et al., 2017). It is probably that both the authigenic pyrite connected with biotite, ilmenite or earlier pyrite and the synsedimentary pyrite just play a role of providing a macro or micro reduction environment. Whereas the pyrite related to clay minerals or carbonaceous debris not only acts as reductant, but also provides space for adsorption or replacement of uranium, which fully demonstrates that this types of authigenic pyrite should be formed a bit earlier than uranium minerals during the mineralization stage (Reynolds and Goldhaber, 1983).

Not only could the pyrite (e.g., framboids) adsorb the uranium with high specific surface area (e.g., Fig. 13d), but the pyrite acted as reducing agent needs to be transformed into liquid, and the reducing capacity is determined by the transform speed and amount (Zhao and Shen, 1986). Moreover, the reduction of sulfur is more effective than iron (Xu, 2017), which is in accordance with none Fe-oxides observed in the ore-bearing samples. A great number of simulation experiments proved that the mechanism of reduction of uranium by pyrite was mainly due to the precipitation of uranium minerals by S^{2-} formed by the reaction of pyrite with water under anaerobic microenvironment (e.g., Wersin et al., 1994; Chen and Guo, 2007):

$$S^{2-} + U^{6+} + H_2O \rightarrow U^{4+} + SO_4^{2-} + H^+ \quad (6)$$

In the sandstone-type uranium deposit, different stages of pyrite

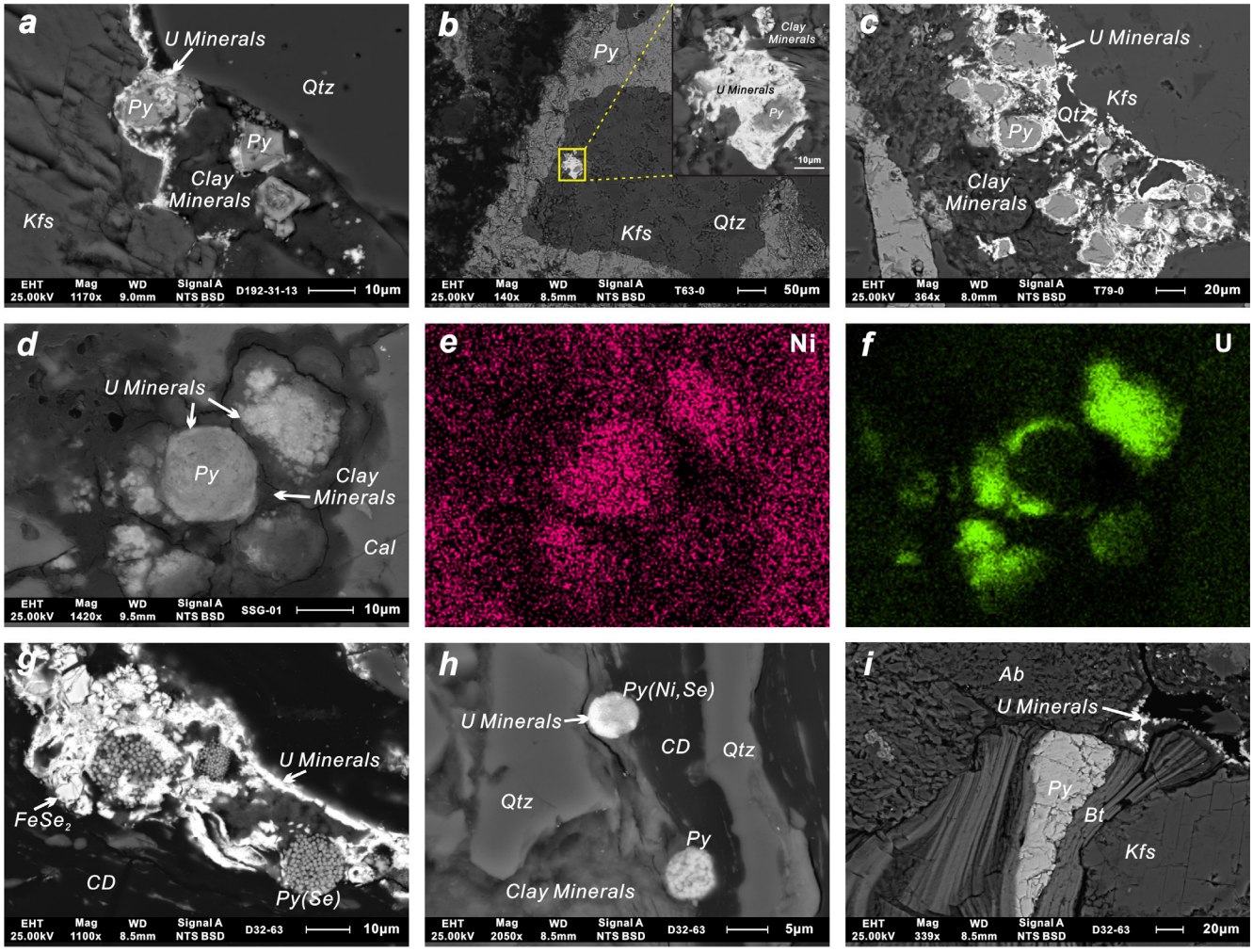

Fig. 13. Occurrence relationship between authigenic pyrite and fine-grained U-bearing minerals. (a)–(c). Uranium minerals overgrowing margins of euhedral pyrite grains (Py) distributed in clay minerals; (d). A portion of uranium minerals replaced the framboidal pyrite (Py), and another are distributed around it; (e). The mapping of Ni of Fig. d; (f). The mapping of U of Fig. d; (g). Uranium minerals intergrow with porous framboidal pyrite (Py) containing minor Se and ferroselite ($FeSe_2$) in carbonaceous debris (CD); (h). U-bearing minerals are replacing the Ni- and Se-bearing framboidal pyrite developed under the combined effect of carbonaceous debris (CD) and clay minerals; (i). Uranium minerals are distributed around the biotite (Bt), and the pyrite (Py) infills the cleavage. Ab-albite, Cal-calcite, Kfs-K-feldspar, Qtz-quartz.

(pre-ore, ore and post-ore) are hosted in the sandbodies together. And the multi-stage pyrite can be distinguished from the morphology observation, chemical composition analyses and large scale heterogeneity of $\delta^{34}S$ compositions, which probably reflect multi-step reactions, including sulfate reduction, pyrite oxidation and reduction (e.g., Rackley, 1972; Reynolds and Goldhaber, 1982). Additionaly, the distribution of trace element in pyrite grains can reflect the geological information of ore forming fluids or diagenetic fluids and facilitate to separate its forming periods (e.g., Ingham et al., 2014; Chu et al., 2015; Lach et al., 2015). However, there is an indistinct boundary line between uranium mineralization and the diagenesis. In the process of diagenesis, there are multiple components contributed to the formation of authigenic pyrite coefficiently, and each has a different role to make pyrite crystallized and precipitated around or in them (Fig. 14).

6. Conclusions

(1) Authigenic pyrite during diagenesis is closely related to carbonaceous debris, clay minerals, biotite, the earlier pyrite, and ilmenite, and the distribution pattern of pyrite is classified as: (i) periphery; (ii) infilling; (iii) the combined form of the above two.
(2) *In situ* $\delta^{34}S$ values of the authigenic pyrite range from −47.0‰ to −19.2‰ associated with carbonaceous debris, −2.8‰ to +19.1‰ with clay minerals, −37.8‰ to +8.4‰ with biotite, +18.2‰ to +18.3‰ with ilmenite, and −52.5‰ and +35.4‰ with uranium minerals, indicating different sources of sulfur including biogenic origin associated with BSR process and hydrothermal source in an open system.
(3) Both the authigenic pyrite related to carbonaceous debris and clay minerals are most closely associated with the uranium minerals as absorbent and reductant, and the reduction of sulfur is more effective than iron, and the pyrite may be formed a bit earlier than uranium minerals during the mineralization stage.

Acknowledgements

This study was supported by the Deep Land Resources Exploration and Exploitation Project (2018YFC0604202), 973 Project (2015CB453003), the Geological Survey Foundation of Ministry of Finance of the People's Republic of China (12120115013701), Fundamental Research Funds for the Central Universities, China University of Geosciences (Wuhan) (No. G1323511660) and National Natural Science Foundation of China (No. 41502105), from China. We are grateful to Xiaoquan Jiao, Aisheng Miao, Gui Wang and other

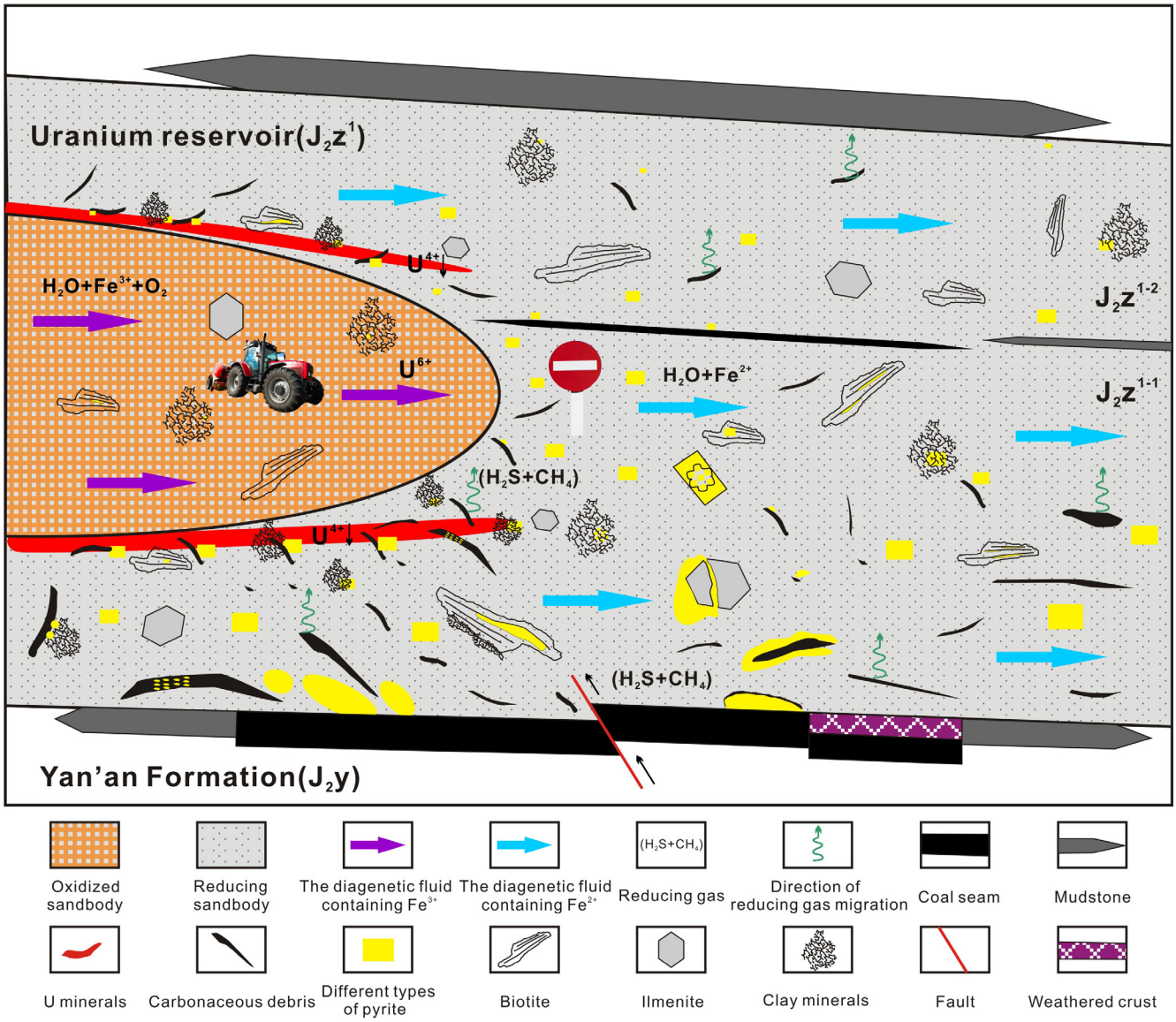

Fig. 14. The model of both forming process and occurrence characteristics of authigenic pyrite during diagenesis in uranium reservoir sandbodies.

workers from the Geolocical Party No.208, CNNC for help with the field work. We also ackownledge the effort of Xujie Guo and Fan Zhang for their help in simpling and testing. Yonggao Guo is thanked for language polishing.

Appendix A. Supplementary data

Supplementary data to this article can be found online at https://doi.org/10.1016/j.oregeorev.2019.03.003.

References

Akhtar, S., Yang, X., Pirajno, F., 2017. Sandstone type uranium deposits in the Ordos Basin, Northwest China: a case study and an overview. J. Asian Earth Sci. 146, 367–382.

Aplin, A.C., Coleman, M.L., 1995. Sour gas and water chemistry of the Bridport sands reservoir, Wytch Farm, UK. Geol. Soc. London Spec. Publ. 86, 303–314.

Beier, J.A., Feldman, H.R., 1991. Sulfur isotopes and paragenesis of sulfide minerals in the Silurian Waldron Shale, southern Indiana. Geology 19, 389–392.

Butler, I.B., Rickard, D., 2000. Framboidal pyrite formation via the oxidation of iron (II) monosulfide by hydrogen sulphide. Geochim. Cosmochim. Acta 64, 2665–2672.

Cai, C.F., Worden, R.H., Wang, Q.H., Xiang, T.S., Zhu, J.Q., Chu, X.L., 2002. Chemical and isotopic evidence for secondary alteration of natural gases in the Hetianhe Field, Bachu Uplift of the Tarim Basin. Org Geochem. 33, 1415–1427.

Cai, C.F., Li, H.T., Qin, M.K., Luo, X.R., Wang, F.Y., Ou, G.X., 2007. Biogenic and petroleum-related ore-forming processes in Dongsheng uranium deposit, NW China. Ore Geol. Rev. 32, 262–274.

Cai, C.F., Li, H.T., Li, K.K., Lei, J., 2008. Anaerobic oxidation of petroleum coupled with reduction of uranium mineralization – cases from dongsheng and qianjiadian uranium deposits. Petrol. Geol. Exp. 30, 518–521 (in Chinese with English abstract).

Canfield, D.E., Raiswell, R., Bottrell, S.H., 1992. The reactivity of sedimentary iron minerals toward sulfide. Am. J. Sci. 292, 659–683.

Chambers, L.A., Trudinger, P.A., 1979. Microbiological fractionation of stable sulfur isotopes: a review and critique. Geomicrobiol J. 1, 249–293.

Chen, H.B., Xu, G.Z., Wang, J.P., Li, W.H., Zhao, X.G., 2006a. Mineralization characteristics of Diantou uranium deposit in the southern margin of Ordos and in comparison with Dongsheng uranium deposit. Acta Geol. Sin. 80, 724–732 (in Chinese with English abstract).

Chen, R.Y., Luo, X.R., Chen, Z.K., Yu, J., Yang, Y., 2006b. Restoration of burial history of four periods in Ordos Basin. Acta Petrolei Sinica 27, 43–47 (in Chinese with English abstract).

Chen, Z.Y., Guo, Q.Y., 2007. Mechanism of U-reduction and concentration by sulphides at sandstone type uranium deposits. Uranium Geol. 23, 321–1315 (in Chinese with English abstract).

Chen, Y., Cheng, H.F., Deng, Y.T., Lin, Y., 2015. Progress in uranium adsorption by clay minerals. Geol. Chem. Min. 37, 93–98 (in Chinese with English abstract).

Chen, C., Liu, H.J., Hou, H.Q., Han, S.Y., Ke, D., Bai, Y.S., Ou, G.X., Li, Y.R., 2016. The relationship between pyrite and sandstone-hosted uranium mineralization of the Zhiluo Formation in the northern Ordos Basin. Acta Geol. Sin. 90, 3375–3380 (in Chinese with English abstract).

Chen, L.L., Feng, X.X., Sima, X.Z., Li, J.G., Guo, H., Chen, Y., Zhao, H.L., Teng, C., Wang, G., Liu, Z.R., Li, S.G., 2017. Occurrence forms of the uranium minerals in the

Nalinggou area of the Ordos Basin and Geological implications. Geol. Exploration 53, 632–642 (in Chinese with English abstract).
Chu, H., Chi, G.X., Bosman, S., Card, C., 2015. Diagenetic and geochemical studies of sandstones from drill core DV10-001 in the Athabasca basin, Canada, and implications for uranium mineralization. J. Geochem. Explor. 148, 206–230.
Coplen, T.B., Bohlke, J.K., De Bievre, P., Ding, T., Holden, N.E., Hopple, J.A., Krouse, H.R., Lamberty, A., Peiser, H.S., Revese, K., Rieder, S.E., Rosman, K.J.R., Roth, E., Taylor, P.D.P., Vocke Jr, R.D., Xiao, Y.K., 2002. Isotope-abundance variations of selected elements (IUPAC Technical Report). Pure Appl. Chem. 74, 1987–2017.
Deditius, A.P., Utsunomiya, S., Ewing, R.C., 2008. The chemical stability of coffinite, USiO4·nH2O; 0 < n < 2, associated with organic matter: A case study from Grants uranium region, New Mexico, USA. Chem. Geol. 251, 33–49.
Eglizaud, N., Miserque, F., Simoni, E., Schlegel, M., Descostes, M., 2006. Uranium(VI) interaction with pyrite (FeS_2): chemical and spectroscopic studies. Radiochim. Acta 94, 651–656.
Gallegos, T.J., Campbell, K.M., Zielinski, R.A., Reimus, P.W., Clay, J.T., Janot, N., Bargar, J.R., Benzel, W.M., 2015. Persistent U(IV) and U(VI) following in-situ recovery (ISR) mining of a sandstone uranium deposit, Wyoming, USA. Appl. Geochem. 63, 222–234.
Goldhaber, M.B., Hemingway, B.S., Mohagheghi, A., Reynolds, R.L., Northrop, H.R., 1987. Origin of coffinite in sedimentary rocks by a sequential adsorption-reduction mechanism. Bulletin De Mineralogie 110, 131–144.
Granger, H.C., Warren, C.G., 1974. Zoning in the Altered Tongue Associated with Roll-Type Uranium Deposits. Internantional Atomic Energy Agency, Vienna, pp. 185–199.
Guevremont, J.M., Strongin, D.R., Schoonen, M.A.A., 1998. Thermal chemistry of H_2S and H_2O on the (100) plane of pyrite: Unique reactivity of defect sites. Am. Mineral. 83, 1246–1255.
Han, X.Z., Zhang, Z.L., Yao, C.L., Li, X.D., Li, S.X., Miao, A.S., Yang, J.X., 2008. Discussion on metallogenic model for sandstone-hosted uranium deposits in northeastern Ordos Basin. Mineral Deposits 27, 415–422 (in Chinese with English abstract).
Holser, W.T., 1977. Catastrophic chemical event in history of the ocean. Nature 267, 403–408.
Huang, J.B., Li, S.X., 2007. Metallogenic characteristics, model and exploration prospect for the paleo-interlayer-oxidation type sandstone-hosted uranium deposits in China. Uranium Geol. 23, 7–16 (in Chinese with English abstract).
Ingham, E.S., Cook, N.J., Cliff, J., Ciobanu, C.L., Huddleston, A., 2014. A combined chemical, isotopic and microstructural study of pyrite from roll-front uranium deposits, Lake Eyre Basin, South Australia. Geochim. Cosmochim. Acta 125, 440–465.
Jaireth, S., Clarke, J., Cross, A., 2010. Exploring for sandstone-hosted uranium deposits in paleovalleys and paleochannels. Geoscience Australia Ausgeo News 97, 1–5.
Jensen, M.L., 1958. Sulfur isotopes and the origin of sandstone-type uranium deposits. Econ. Geol. Bull. Soc. Econ. Geol. 53, 598–616.
Jiang, S.Y., Ling, H.F., 2004. Stable isotope geochemistry. In: Chen, J., Wang, H.N. (Eds.), Geochemistry. Science Press, Beijing, pp. 129–141 (in Chinese with English abstract).
Jiang, Y.F., Qian, H.D., Zhou, G.Q., 2016. Mineralogy and geochemistry of different morphological pyrite in Late Permian coals, South China. Arabian J. Geosci. 9, 590–607.
Jiao, Y.Q., Chen, A.P., Wang, M.F., Wu, L.Q., Yuan, H.T., Yang, Q., Zhang, C.Z., Xu, Z.C., 2005a. Genetic analysis of the bottom sandstone of Zhiluo Formation, northeastern Ordos Basin: predictive base of spatial orientation of sandstone-type uranium deposit. Acta Sedimentol. Sin. 23, 371–379 (in Chinese with English abstract).
Jiao, Y.Q., Wu, L.Q., Wang, M.F., Xu, Z.C., 2005b. Forecasting the occurrence of sandstone-type uranium deposits by spatial analysis: An example from the northeastern Ordos Basin, China. In: Mao, J.M., Bierlein, F.P. (Eds.), Mineral Deposit Reaserch: Meeting the Global Challenge. Springer-Verlag, Berlin Heidelberg, pp. 273–275.
Jiao, Y.Q., Wu, L.Q., Yang, Q., 2007. Uranium reservoir: a new concept of sandstone-type uranium deposits geology. Geol. Sci. Technol. Inf. 26, 1–7 (in Chinese with English abstract).
Jiao, Y.Q., Wu, L.Q., Rong, H., Peng, Y.B., Miao, A.S., Wang, X.M., 2016. The relationship between Jurassic coal measures and sandstone-type uranium deposits in the northeastern Ordos Basin, China. Acta Geol. Sin. 90, 2117–2132.
Jiao, Y.Q., Wu, L.Q., Rong, H., Zhang, F., Yue, L., Tao, Z.P., Sun, Y.H., 2018. Geological modeling of uranium reservoir: The geological foundation of revealing the metallogenic mechanism and solving “Remaining Uranium”. Earth Sci. 43, 3568–3583 (in Chinese with English abstract).
Jobson, A.M., Cook, F.D., Westlake, D.W.S., 1979. Interaction of aerobic and anaerobic bacteria in petroleum biodegradation. Chem. Geol. 24, 355–465.
Johnston, D.T., 2011. Multiple sulfur isotopes and the evolution of Earth's surface sulfur cycle. Earth Sci. Rev. 106, 161–183.
Kohn, M.J., Riciputi, L.R., Stakes, D., Orange, D.L., 1998. Sulfur isotope variability in biogenic pyrite: reflections of heterogeneous bacterial colonization. Am. Mineral. 83, 1454–1468.
Kortenski, J., Kostova, I., 1996. Occurrence and morphology of pyrite in Bulgarian coals. Int. J. Coal Geol. 29, 273–290.
Lach, P., Cathelineau, M., Brouand, M., Fiet, N., 2015. In-situ isotopic and chemical study of pyrite from Chu-Sarysu (Kazakhstan) roll-front uranium deposit. Procedia Earth Planet. Sci. 13, 207–210.
Laduke, J., 2013. Geochemistry and mineralogy of the alteration halo associated with the Three Crow roll-front uranium deposit, Nebraska, USA. Dissertations Theses – Gradworks 49, 22.
Li, D.H., 2007. Coal seams and strata correlation in Ulan Xil district, Dongsheng coalfield. Coal Geol. China 19, 157–160 (in Chinese with English abstract).
Li, Z.Y., Chen, A.P., Fang, X.H., Ou, G.X., Xia, Y.L., Sun, Y., 2008. Origin and superposition metallogenic model of the sandstone–type uranium deposit in the northeastern Ordos Basin, China. Acta Geol. Sin. 82, 745–749.
Li, W.H., Xu, G.Z., 2006. Relationship between late reformation and formation of sandstone type uranium ore in Ordos Basin. J. Earth Sci. Environ. 28, 19–23 (in Chinese with English abstract).
Liang, R., Chi, G.X., Ashton, K., Blamey, N., Fayek, M., 2017. Fluid compositions and P-T conditions of vein-type uranium mineralization in the Beaverlodge uranium district, northern Saskatchewan, Canada. Ore Geol. Rev. 80, 460–483.
Liu, S.F., 1998. The coupling mechanism of basin and orogen in the western Ordos Basin and adjacent regions of China. J. Asian Earth Sci. 16, 369–383.
Liu, J.H., Shi, W.J., Sun, Z.X., 2007. A study of the formation process and ore prospecting indicators of the sandstone type uranium deposits in the light of uranium series isotopes. Acta Geoscientica Sinica 28, 39–42 (in Chinese with English abstract).
Love, L.G., 1971. Early diagenetic polyframboidal pyrite, primary and redeposited, from the Wenlockian Denbigh Grit Group, Conway, north Wales, U.K. J. Sediment. Res. 41, 1038–1044.
Lovley, D.R., Phillips, E.J.P., Gorby, Y.A., Landa, E.R., 1991. Microbial reduction of uranium. Nature 350, 413–416.
Ma, Y., Wu, B.L., Liu, Y.F., Liu, C.Y., Zhao, Z.P., Wang, H.T., Song, Z.S., Wei, A.J., 2013. Study on uranium occurrence state of sandstone-type uranium deposits in HJQ region, Ordos Basin. Northwestern Geol. 46, 141–152 (in Chinese with English abstract).
Miao, A.S., Lu, Q., Liu, H.F., Xiao, P., 2009. Occurrence and formation of coffinite in ancient interlayer oxidizing zone of sandstone type U-deposit in Ordos Basin. Geol. Sci. Technol. Inf. 28, 51–58 (in Chinese with English abstract).
Miao, A.S., Jiao, Y.Q., Chang, B.C., Wu, L.Q., Rong, H., Liu, Z.B., 2010a. Detailed investigation of the paleo-interlayer-oxidation zone of Dongsheng uranium deposit in northeastern Ordos Basin. Geol. Sci. Technol. Inf. 29, 55–61 (in Chinese with English abstract).
Miao, A.S., Lu, Q., Liu, H.F., Xiao, P., 2010b. Electronic microscopy study on the uranium minerals of Dongsheng sandstone-type uranium deposit in Ordos Basin. Geoscience 24, 785–792 (in Chinese with English abstract).
Min, M.Z., Chen, J., Wang, J.P., Wei, G.H., Fayek, M., 2005a. Mineral paragenesis and textures associated with sandstone-hosted roll-front uranium deposits, NW China. Ore Geol. Rev. 26, 51–69.
Min, M.Z., Xu, H.F., Chen, J., Fayek, M., 2005b. Evidence of uranium biomineralization in sandstone-hosted roll-front uranium deposits, northwestern China. Ore Geol. Rev. 26, 198–206.
Nash, J.T., Granger, H.C., Adams, S.S., 1981. Geology and concepts of genesis of important types of uranium deposits. Econ. Geol. 63–116 75th ann. vol.
Northrop, H.R., Goldhaber, M.B., 1990. Genesis of the tabular-type vanadium-uranium deposits of the Henry Basin, Utah. Am. Political Sci. Rev. 94, 727–730.
Qafoku, N.P., Kukkadapu, R.K., Mckinley, J.P., Arey, B.W., Kelly, S.D., Wang, C.M., Resch, C.T., Long, P.E., 2009. Uranium in framboidal pyrite from a naturally bioreduced alluvial sediment. Environ. Sci. Technol. 43, 8528–8534.
Qiao, H.M., Xu, G.Z., Zhang, F.X., Shang, G.F., Song, Z., Liu, Z.G., 2013. Study on iron geochemical behavior in the interlayer oxidation zone sandstone-type uranium metallogenetic process: a case from Shihongtan uranium deposit in the Turpan-Hami basin of Xinjiang. Acta Sedimentol. Sin. 31, 461–467 (in Chinese with English abstract).
Rackley, R.I., 1972. Environment of Wyoming Tertiary uranium deposits. AAPG Bull. 56, 755–774.
Raiswell, R., 1982. Pyrite texture, isotopic composition and the availability of iron. Am. J. Sci. 282, 1244–1263.
Raiswell, R., Berner, R.A., 1985. Pyrite formation in euxinic and semi-euxinic sediments. Am. J. Ofence 285, 710–724.
Raiswell, R., 1997. A geochemical framework for the application of stable sulphur isotopes to fossil pyritization. J. Geol. Soc. 154, 343–356.
Reynolds, R.L., Goldhaber, M.B., 1982. Biogenic and nonbiogenic ore-forming processes in the South Texas uranium district: evidence from the Panna Maria deposit. Econ. Geol. 77, 541–556.
Reynolds, R.L., Goldhaber, M.B., 1983. Iron disulfide minerals and the genesis of roll-type uranium deposits. Econ. Geol. 78, 105–120.
Rickard, D., 1997. Kinetics of pyrite formation by the H_2S oxidation of iron (II) monosulphide in aqueous solutions between 25°C and 125°C: the rate equation. Geochim. Cosmochim. Acta 61, 115–134.
Riegler, T., Beaufort, M.F., Allard, T., Pierson-Wickmann, A.C., Beaufort, D., 2016. Nanoscale relationships between uranium and carbonaceous material in alteration halos around unconformity-related uranium deposits of the Kiggavik camp, Paleoproterozoic Thelon Basin, Nunavut, Canada. Ore Geol. Rev. 79, 382–391.
Ritts, B.D., Hanson, A.D., Darby, B.J., Nanson, L., Berry, A., 2004. Sedimentary record of Triassic intraplate extension in north China: Evidence from the nonmarine NW Ordos Basin, Helan Shan and Zhuozi Shan. Tectonophysics 386, 177–202.
Rong, H., Jiao, Y.Q., Wu, L.Q., Ji, D.M., Li, H.L., Zhu, Q., Cao, M.Q., Wang, X.M., Li, Q.C., Xie, H.L., 2016. Epigenetic alteration and its constraints on uranium mineralization from the Qianjiadian uranium deposit, southern Songliao Basin. Earth Sci. 41, 153–166 (in Chinese with English abstract).
Sawlowicz, Z., 1993. Pyrite framboids and their development: a new conceptual mechanism. Geol. Rundsch. 82, 148–156.
Sawłowicz, Z., 2000. Framboids: from their origin to application. Polish Academy of Science, Div. Krakow, pp. 1–80.
Scott, T.B., Tort, O.R., Allen, G.C., 2007. Aqueous uptake of uranium onto pyrite surfaces; reactivity of fresh versus weathered material. Geochim. Cosmochim. Acta 71, 5044–5053.
Scott, R.J., Meffre, S., Woodhead, J., Gilbert, S.E., Berry, R.F., Emsbo, P., 2009. Development of framboidal pyrite during diagenesis, low-grade regional metamorphism, and hydrothermal alteration. Econ. Geol. 104, 1143–1168.
Seal, R.R., 2006. Sulfur isotope geochemistry of sulfide minerals. Rev. Mineral. Geochem. 61, 633–677.

Shikazono, N., 1999. Compositional variation of pyrite, diagenetic alteration and genesis of Tono sandstone-type uranium deposits in Japan. Resour. Geol. 20, 55–64.
Spirakis, C.S., 1996. The roles of organic matter in the formation of uranium deposits in sedimentary rocks. Ore Geol. Rev. 11, 53–69.
Sun, Y., 2016. Organic geochemical zonation characteristics of sandstone-type uranium deposit and its relation to metallization – a case study of Zaohuohao uranium deposit in Inner Mongolia. Uranium Geol. 32, 129–136 (in Chinese with English abstract).
Sweeney, R.E., Kaplan, I.R., 1973. Pyrite framboid formation; Laboratory synthesis and marine sediments. Econ. Geol. 68, 618–634.
Taylor, K.G., Macquaker, J.H.S., 2000. Early diagenetic pyrite morphology in a mudstone-dominated succession: the Lower Jurassic Cleveland Ironstone Formation, eastern England. Sed. Geol. 131, 77–86.
Ulrich, G.W., Stefano, M.B., Michael, E.B., 2001. Hypersulfidic deep biosphere indicates extreme sulfur isotope fractionation during single-step microbial sulfate reduction. Geology 29, 647–650.
Wang, A.L., Zhao, Y.G., 2012. The authigenic clay mineral research status, contents and methods of sandstone. Sci. Technol. Inf. 30, 53–55 (in Chinese with English abstract).
Warren, C.G., 1971. Method for discriminating between biogenic and chemical origins of the ore-state pyrite in a roll-type uranium. Econ. Geol. 66, 919–928.
Warren, C.G., 1972. Sulfur isotopes as a clue to the genetic geochemistry of a roll-type uranium deposit. Econ. Geol. 67, 759–767.
Wei, H.Y., Chen, D.Z., Wang, J.G., Hao, Y., Tucker, M.E., 2013. Organic accumulation in the lower Chihsia Formation (Middle Permian) of South China: constraints from pyrite morphology and multiple geochemical proxies. Inst. Geol. Geophys., Chinese Acad. Sci. 353–355, 73–86 (in Chinese with English abstract).
Wei, H.Y., Algeo, T.J., Yu, H., Wang, J.G., Guo, C., Shi, G., 2015. Episodic euxinia in the Changhsingian (late Permian) of South China: evidence from framboidal pyrite and geochemical data. Sed. Geol. 319, 78–97.
Wei, H.Y., Wei, X.M., Qiu, Z., Song, H.Y., Guo, S., 2016. Redox conditions across the G-L boundary in South China: evidence from pyrite morphology and sulfur isotopic compositions. Chem. Geol. 440, 1–14.
Wersin, P., Hochella Jr, M.F., Persson, P., Redden, G., Leckie, J.O., Harris, D.W., 1994. Interaction between aqueous uranium(VI) and sulfide minerals: spectroscopic evidence for sorption and reduction. Geochim. Cosmochim. Acta 58, 2829–2843.
Wignall, P.B., Vedrine, S., Bond, D.P., Lai, X.L., Ali, J.R., Jiang, H., 2009. Facies analysis and sea-level change at the Guadalupian-Lopingian Global Stratotype (Laibin, South China), and its bearing on the end-Guadalupian mass extinction. J. Geol. Soc. 166, 655–666.
Wu, B.L., Zhang, W.Y., Song, Z.S., Cun, X.N., Sun, L., Luo, J.J., Li, Y.Q., Cheng, X.H., Sun, B., 2016. Geological and geochemical characteristics of uranium minerals in the sandstone-type uranium deposits in the north of Ordos Basin and their genetic significance. Acta Geol. Sin. 90, 3393–3407 (in Chinese with English abstract).
Wulser, P.A., Brugger, J., Foden, J., Pfeifer, H.R., 2011. The sandstone-hosted Beverley uranium deposit, Lake Frome Basin, south Australia: mineralogy, geochemistry, and a time-constrained model for its genesis. Econ. Geol. 106, 835–867.
Xiang, W.D., Fang, X.H., Li, T.G., Chen, X.L., Pang, Y.Q., Cheng, H.H., 2005. Geology and origin of the Dongsheng uranium deposit in the Ordos Basin, north China. Mineral Deposit Research: Meeting the Global Challenge. Springer, Germany, pp. 327–330.
Xiang, W.D., Fang, X.H., Li, T.G., Chen, X.L., Pang, Y.Q., Cheng, H.H., 2006. Metallogenic characteristics and model of Dongsheng uranium deposit in Ordos Basin, north China. Uranium Geol. 22, 257–266 (in Chinese with English abstract).
Xiao, X.J., Li, Z.Y., Fang, X.H., Ou, G.X., Sun, Y., Chen, A.P., 2004. The evidences and significances of epithermal mineralization fluid in the Dongsheng sandstone type uranium deposit. Bullet. Mineral. Petrol. Geochem. 23, 301–304 (in Chinese with English abstract).
Xie, H.L., 2016. Water-rock interaction in the forming of the paleo-interlayer oxidation zone of the Daying uranium deposit, northern Ordos Basin. China Univ. Geosci. (in Chinese with English abstract).
Xing, X.J., Liu, Y.Q., Li, W.H., Gong, B.L., 2008. Sandstone diagenesis and uranium mineralization of the Zhiluo Formation in the Diantou area, southern Ordos Basin. Acta Geoscientica Sinica 29, 179–188 (in Chinese with English abstract).
Xu, Z.L., 2017. Study on the mechanism of U(VI) on the surface of pyrite and hydroxyapatite. East China Univ. Technol. (in Chinese with English abstract).
Xue, C.J., Chi, G.X., Xue, W., 2010. Interaction of two fluid systems in the formation of sandstone-hosted uranium deposits in the Ordos Basin: geochemical evidence and hydrodynamic modeling. J. Geochem. Explor. 106, 226–235.
Xue, C.J., Chi, G.X., Xue, W., 2011. Effects of hydrocarbon generation on fluid flow in the Ordos Basin and its relationship to uranium mineralization. Geosci. Front. 2, 439–447.
Yang, X.Y., Ling, M.X., Sun, W.D., Luo, X.D., Lai, X.D., Liu, C.Y., Miao, J.Y., Sun, W., 2009a. The genesis of sandstone-type uranium deposits in the Ordos Basin, NW China: constraints provided by fluid inclusions and stable isotopes. Int. Geol. Rev. 51, 422–455.
Yang, X.Y., Ling, M.X., Lai, X.D., Sun, W., Liu, C.Y., 2009b. Uranium mineral occurrence of sandstone-type uranium deposits in the Dongsheng-Huanglong region, Ordos Basin. Acta Geol. Sin. 83, 1167–1177 (in Chinese with English abstract).
Yi, C., Chen, X.L., Li, X.D., Zhang, K., Wang, M.T., Li, J.X., 2015a. Metallogenic characteristic of the paleo-interlayer oxidation type sandstone-hosted uranium deposits in northeastern Ordos Basin. Uranium Geol. 31, 247–257 (in Chinese with English abstract).
Yi, C., Gao, H.W., Li, X.D., Zhang, K., Chen, X.L., Li, J.X., 2015b. Study on indicative significance of major elements for sandstone-type uranium deposit in Zhiluo Formation in northeastern Ordos Basin. Mineral Deposits 34, 801–813 (in Chinese with English abstract).
Yi, C., Li, X.D., Zhang, K., Wang, G., Wang, Y.J., Wang, M.T., 2017. Relationship between reducing materials and uranium mineralization in the northeastern Ordos Basin. Geol. Rev. 63, 139–140 (in Chinese).
Zhang, Z.L., Han, X.Z., Li, S.X., Yao, C.L., Zhao, Y.A., 2010. Sedimentary facies of the lower part of Middle Jurassic Zhiluo Formation in northeastern Ordos Basin and its controls on uranium mineralization. J. Palaeogeogr. 12, 749–758 (in Chinese with English abstract).
Zhang, L., Liu, C.Y., Fayek, M., Wu, B.L., Lei, K.Y., Cun, X.N., Sun, L., 2017. Hydrothermal mineralization in the sandstone–hosted Hangjinqi uranium deposit, North Ordos Basin, China. Ore Geol. Rev. 80, 103–115.
Zhang, F., Jiao, Y.Q., Wu, L.Q., Rong, H., Wang, L.H., 2018. Relations of uranium enrichment and carbonaceous debris within the Daying uranium deposit, northern Ordos Basin. J. Earth Sci. https://doi.org/10.1007/s12583-017-0952-0.
Zhao, F.M., Shen, C.Q., 1986. Experimental researches on paragenetic condition for pyrite and pitchblende and its role in pitchblende formation. Uranium Geol. 2, 3–9 (in Chinese with English abstract).
Zhao, H.G., Ou, G.X., 2006. The relationship between depositional system and ore-formation of sandstone-type uranium deposits in Dongsheng area, Ordos basin. Uranium Geol. 22, 136–198 (in Chinese with English abstract).
Zhao, J., Liang, J.L., Long, X.P., Li, J., Xiang, Q.R., Zhang, J.C., Hao, J.L., 2018. Genesis and evolution of framboidal pyrite and its implications for the ore-forming process of Carlin-style gold deposits, southwestern China. Ore Geol. Rev. 102, 426–436.